Piñeiro-López, L.; Valverde-Muñoz, FJ.; Seredyuk, M.; Muñoz Roca, MDC.; Haukka, M.; Real, JA. (2017). Guest Induced Strong Cooperative One- and Two-Step Spin Transitions in Highly Porous Iron(II) Hofmann-Type Metal-Organic Frameworks. Inorganic Chemistry. 56(12):7038-7047. https://doi.org/10.1021/acs.inorgchem.7b00639

Guest Induced Strong Cooperative One- and Two-Step Spin Transitions in Highly Porous Iron(II) Hofmann-Type Metal−Organic Frameworks

Lucía Piñeiro-Lopez,[†] Francisco Javier Valverde-Muñoz,[†] Maksym Seredyuk,*[,†,‡] M. Carmen Muñoz,[§] Matti Haukka,[∥] and José Antonio Real*[,†]

[†]Institut de Ciencia Molecular (ICMol), Departament de Química Inorganica, Universitat de Valencia, C/Catedratico José Beltrán Martínez, 2, 46980 Paterna (Valencia), Spain

[‡]Taras Shevchenko National University, Department of Physical Chemistry, Volodymyrska Str. 64, Kyiv 01601, Ukraine

[§]Departament de Física Aplicada, Universitat Politecnica de Valencia, Camino de Vera s/n, E-46022, Valencia, Spain

[∥]Department of Chemistry, University of Jyvaskylä FIN-40014, Jyvaskylä, Finland

Supporting Information

ABSTRACT: The synthesis, crystal structure, magnetic, calorimetric, and Mössbauer studies of a series of new Hofmann-type spin crossover (SCO) metal−organic frameworks (MOFs) is reported. The new SCO-MOFs arise from self-assembly of Fe^{II}, bis(4-pyridyl)butadiyne (bpb), and $[Ag(CN)_2]^-$ or $[M^{II}(CN)_4]^{2-}$ (M^{II} = Ni, Pd). Interpenetration of four identical 3D networks with α-Po topology are obtained for $\{Fe(bpb)[Ag^I(CN)_2]_2\}$ due to the length of the rod-like bismonodentate bpb and $[Ag(CN)_2]^-$ ligands. The four networks are tightly packed and organized in two subsets orthogonally interpenetrated, while the networks in each subset display parallel interpenetration. This nonporous material undergoes a very incomplete SCO, which is rationalized from its intricate structure. In contrast, the single network Hofmann-type MOFs $\{Fe(bpb)[M^{II}(CN)_4]\}\cdot n$Guest ($M^{II}$ = Ni, Pd) feature enhanced porosity and display complete one-step or two-step cooperative SCO behaviors when the pores are filled with two molecules of nitrobenzene or naphthalene that interact strongly with the pyridyl and cyano moieties of the bpb ligands via π−π stacking. The lack of these guest molecules favors stabilization of the high-spin state in the whole range of temperatures. However, application of hydrostatic pressure induces one- and two-step SCO.

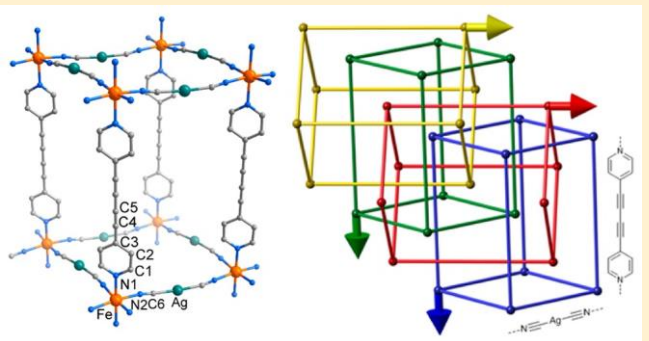

INTRODUCTION

Much interest in the area of material sciences is focused on the search for new molecular materials displaying switchable physical properties controlled by external stimuli, as they can be basic components in the design of technologically valuable molecular devices.[1] Fe^{II} complexes that exhibit spin crossover (SCO) between the high-spin (S = 2; HS) and the low-spin (S = 0; LS) states are among the most studied families of switchable molecular materials. The HS↔LS spin state change is reversible and detectable and occurs with concomitant variation of relevant physical magnitudes including magnetic susceptibility, color, dielectric constant, and electric conductivity, controlled by the action of temperature, pressure, light, and analytes.[2] The HS↔LS electronic reorganization associated with the SCO is strongly coupled with structural changes at the Fe^{II} centers, which, in favorable conditions, are transmitted to the neighboring Fe^{II} centers in a cooperative way.

Cooperativity may be achieved when the Fe^{II} centers are strongly coupled in the crystal, a fact that confers bistability to the physical properties, one of the most appealing features of SCO materials. The use of rigid coordination bonds as connectors between Fe^{II} SCO centers fueled the so-called polymeric approach, developed in the 1990s, and afforded an important number of 1−3D SCO coordination polymers.[3] In this context, we reported the first 3D Hofmann SCO coordination polymers, $\{Fe(pz)[M^{II}(CN)_4]\}\cdot$Guest (pz = pyrazine; M^{II} = Ni, Pd, Pt) and $\{Fe(L)_x[Ag^I(CN)_2]_2\}$ (L = pz (x = 1), 4,4′-bipyridine (x = 2), tvp (x = 2)).[4] Then, this study was extended to new $\{Fe(L)[M^{II}(CN)_4]\}\cdot$Guest clathrate systems derived from bismonodentate pyridine-like ligands (L) other than pyrazine. Interestingly, this work originated an isoreticular series of 3D SCO porous metal−organic frameworks (SCO-MOFs; see Scheme 1) which represents an interesting example of modulation of the accessible volume in the LS state: 63.3 $Å^3$ (18.1% of the unit cell volume) for pz;[5] 270−290 $Å^3$ (40−42%)

Scheme 1. Illustration of the Two Types of Hofmann-like SCO-MOFs and Bismonodentate Pillar Ligands Employed (M^{II} = Ni, Pd, Pt; M^{I} = Ag, Au)[a]

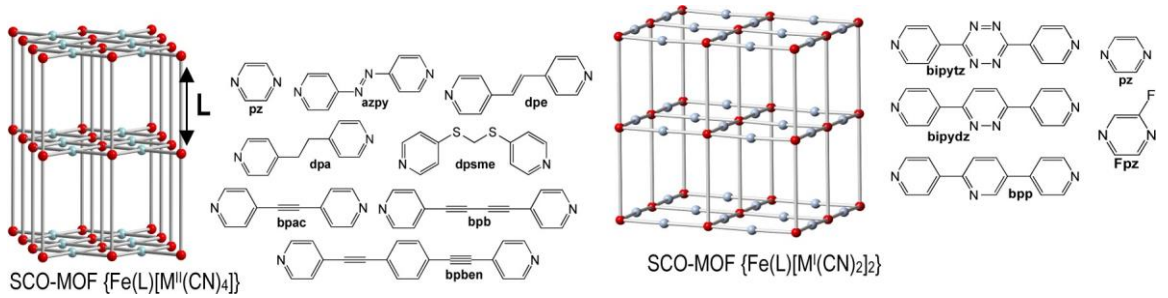

[a]Color code: (red = Fe^{II}; gray = M^{I}, M^{II}).

for bpe,[6] azpy,[7] and bpac;[8] 511 Å^3 (48.9%) for bpeben;[9] and 692.9 Å^3 (49%) for dpsme.[10] More importantly, this series provided a very rich variety of relevant examples in which host−guest interactions influence the cooperative nature of the SCO, i.e., hysteresis width and/or critical temperatures.[11]

The $\{Fe(L)[M^{I}(CN)_2]_2\}\cdot$Guest ($M^{I}$ = Ag, Au) system has afforded a more moderate series of isoreticular SCO-MOFs (Scheme 1). Compared with the tetradentate nature of the $[M^{II}(CN)_4]^{2-}$ units, the ditopic linear $[M^{I}(CN)_2]^{-}$ bridges generate much more open structures, thereby favoring interpenetration of two identical frameworks. This limits the degree of porosity; nevertheless, there is enough space between the frameworks to place guest molecules, a fact that has enabled investigation of new relevant host−guest−SCO correlations.[12]

In a recent communication, we reported on the synthesis and characterization of the new SCO-MOF $\{Fe(bpb)[Pt^{II}(CN)_4]\}\cdot$2Guest where bpb is the pillar ligand bis(4-pyridyl)butadiyne (Scheme 1).[13] This ligand provides the largest available volume, ca. 820 Å^3 in the LS, of the isoreticular series $\{Fe(L)[M^{II}(CN)_4]\}\cdot$Guest. Indeed, it hosts two molecules of naphthalene or nitrobenzene. Both clathrates undergo cooperative SCO with large hysteresis. The SCO takes place in two well-defined steps for the naphthalene clathrate, while only one step characterizes the SCO in the nitrobenzene derivative. As a continuation of this preliminary work, herein we report on the magnetic and calorimetric properties of Mössbauer spectra and crystal structures of $\{Fe(bpb)[Ag^{I}(CN)_2]_2\}$ (1Ag) and $\{Fe(bpb)[M^{II}(CN)_4]\}\cdot n$Guest (2M-Guest; M^{II} = Ni, Pd) with $n = 2$ and Guest = naphthalene and nitrobenzene and the synthesis and characterization of the microcrystalline compounds $\{Fe(bpb)_{1.1}[M^{II}(CN)_4]\}\cdot n CH_3OH$ (2M; M^{II} = Ni, Pd, Pt; n is in the interval 0−1).

RESULTS

Synthesis and Thermal Stability. The title compounds have been synthesized by slow diffusion methods in methanol−water solutions. The presence of appropriate guest molecules during the diffusion enables the growth of single crystals of 2M-Guest (M = Ni, Pd). The thermal analysis indicates an occupation of the pores by about two guest molecules per unit formula, in agreement with elemental and crystallographic analyses. These clathrate derivatives show relatively low thermal stability; i.e., nitrobenzene starts to desorb at ca. 346 K (Ni) and 398 K (Pd) while naphthalene starts to desorb at ca. 379 K (Ni) and 400 K (Pd). The system 1Ag was obtained independently of the presence or absence of guest molecules in the diffusion process. The thermogravimetric analysis shows a lack of guest molecules in the framework, which decomposes in one step from 500 K (Figure S1).

The lack of guest molecules other than water−methanol solvent in the diffusion medium favors precipitation of compounds 2M (M = Ni, Pd, and Pt); under these conditions only microcrystalline powders form. Their elemental analyses are consistent with the presence of an excess of bpb by 10% and the presence of 0−1 labile methanol molecules. Thermogravimetric data (Figure S2) show that 2M decompose at ca. 520 K (Ni), 550 K (Pd), and 560 K (Pt), which are very close (ca. 600 K) to that observed for the guest-free network. The three derivatives are isostructural and display essentially the same PXRD pattern as the simulated one for the crystal structure of 2M-Guest (*vide infra*) from which the guest molecules were artificially removed (Figure S3). Particularly significant is the 001 reflection at 2θ = 5.55°, which corresponds to d = 15.836 Å, a distance that matches quite well the separation between planes that contain $\{Fe[M^{II}(CN)_4]\}_n$ layers pillared by the bpb ligand in 2M-Guest (*vide infra*).

Magnetic Properties. The thermal dependence of the $\chi_M T$ product (χ_M is the molar magnetic susceptibility and T, the temperature) was measured at 1 K/min for all derivatives. Figure 1 shows $\chi_M T$ vs T plots for 1Ag and "guest-free" 2Ni, 2Pd, and 2Pt derivatives at 1 bar and at high pressure. Concerning 1Ag, $\chi_M T$ is about 3.50 cm^3 K mol^{-1} at 300 K and remains practically constant down to 206 K. Then it drops to a value of 2.00 cm^3 K mol^{-1} at 75 K, indicating that this derivative undergoes an incomplete spin conversion involving ca. 43% of the Fe^{II} atoms. The spin transition is centered at ca. 130 K. The decrease of $\chi_M T$ below 75 K corresponds to the zero-field splitting of the remaining HS (S = 2) Fe^{II} centers.

The derivatives 2Ni, 2Pd, and 2Pt are essentially HS. However, the onset of a SCO involving ca. 8−13% of HS-to-LS conversion and the effect of zero-field splitting of the HS centers are observed, respectively, upon cooling below 150 and 75 K. These results stimulated the investigation of external hydrostatic pressure effects (up to ca. 8 kbars) on the variable-temperature magnetic susceptibilities of the unloaded derivatives (see Figure 1). The pressure expectedly shifts the equilibrium transition temperature upward [i.e., $T_{1/2}$ = 208 K (2Pd) and 156 K (2Pt)] and increases completeness [67% (2Pd) and 58% for (2Pt)] of the initially incipient HS↔LS transition. Particularly interesting is the appearance of a gradual double step spin transition in 2Ni with $(T_{1/2})_1$ = 287 K and $(T_{1/2})_2$ = 171 K and ca. 74% completeness.

The magnetic properties of guest loaded derivatives 2Ni-naph, 2Ni-phNO$_2$, 2Pd-naph, and 2Pd-phNO$_2$ are shown in Figure 2. The $\chi_M T$ value for 2Ni-naph and 2Pd-naph is about 3.83 cm^3 K

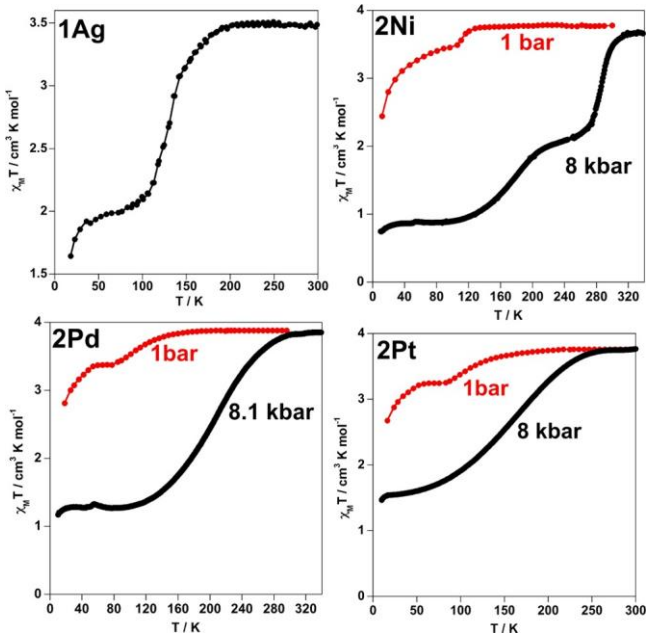

Figure 1. $\chi_M T$ vs T plot for 1Ag and 2Ni, 2Pd, and 2Pt at 1 bar and ca. 8 kbar.

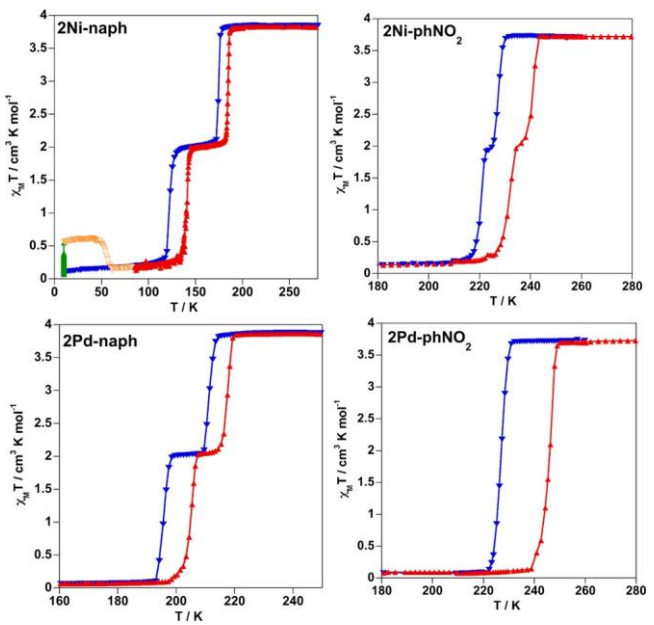

Figure 2. $\chi_M T$ vs T plots for 2Ni-naph, 2Ni-phNO$_2$, 2Pd-naph, and 2Pd-phNO$_2$.

mol^{-1} at 300 K and remains constant down to 179 K (Ni) and 211 K (Pd), then follows an abrupt drop of $\chi_M T$ to 2.0 cm^3 K mol^{-1}, which remains constant in the intervals 172−134 K (Ni) and 209−199 K (Pd). A second drop in $\chi_M T$ occurs upon cooling at temperatures just below 134 K (Ni) and 199 K (Pd) to attain values in the range of 0.1−0.2 cm^3 K mol^{-1}. This complete and cooperative two-step spin transition behavior is characterized by critical temperatures $T_{c1}\downarrow$ = 175.0 K (Ni) and 211.2 K (Pd) and $T_{c2}\downarrow$ = 122.5 K (Ni) and 195.6 K (Pd). In the heating mode, the $\chi_M T$ vs T curves are shifted to higher temperatures and do not match those of the cooling mode, the critical temperatures being $T_{c1}\uparrow$ = 185.0 K (Ni) and 217.5 K (Pd) and $T_{c2}\uparrow$ = 140.0 K (Ni) and 205.0 (Pd). The generated thermal hysteresis for each step are ΔT_{c1} = 10 K (Ni) and 6.3 K (Pd) and ΔT_{c2} = 17.6 (Ni) and 9.4 K (Pd).

The $\chi_M T$ value for 2Ni-NO$_2$ and 2Pd-NO$_2$ is about 3.70 cm^3 K mol^{-1} and practically constant in the interval 300−230 K. Just below 230 K in the cooling mode, the Ni derivative displays two sharp steps separated by a quite narrow plateau (ca. 2 K wide) centered at 224 K and $\chi_M T$ = 1.97 cm^3 K mol^{-1}, while only one complete step transition is observed for the Pd derivative. The critical temperatures are $T_{c1}\downarrow$ = 227.2 K (Ni), $T_{c2}\downarrow$ = 220.6 K (Ni), and $T_c\downarrow$ = 227.0 K (Pd). Similarly to the naphthalene derivatives, the heating mode defines hysteresis loops characterized by $T_{c1}\uparrow$ = 240.8 K (Ni) [ΔT_{c1} = 13.6 K], $T_{c2}\uparrow$ = 231.4 K (Ni) [ΔT_{c2} = 10.8 K], and $T_c\uparrow$ = 246.4 (Pd) [ΔT = 19.4 K]. Table S1 gathers the critical temperatures for the 2M-naph and 2M-phNO$_2$ including the previously reported Pt systems.

Given that 2Ni-naph exhibits the lowest transition temperature, photogeneration of the metastable HS* state at low temperature, the so-called light induced spin state trapping experiment (LIESST) was carried out.[14] Photo excitation of the powdered sample at 10 K with green light over 3 h resulted in an increase of the $\chi_M T$ up to ca. 0.5 cm^3 K mol^{-1}. Upon heating at 0.3 K min^{-1} with a switched off light source, the susceptibility value increases up to ca. 0.62 cm^3 K mol^{-1} at 40 K. This suggests ca. 16% of the Fe^{II} ions undergoing light-induced population of the HS* state. The T_{LIESST} temperature,[15] determined as the inflection point of the curve HS*-to-LS, is 54 K.

Mössbauer Studies. The spin transition in 1Ag and 2Ni-naph was monitored by Mössbauer spectroscopy (Figure 3). For

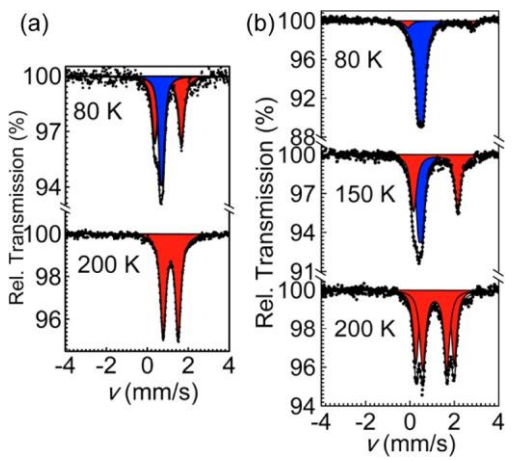

Figure 3. ^{57}Fe Mössbauer spectra for 1Ag (a) and 2Ni-naph (b).

1Ag, the spectra were collected above and below the transition temperature at 200 and 80 K, respectively (Figure 3a). At the higher temperature, the presence of a single doublet with isomer shift ΔE_Q = 1.14(2) mm s^{-1} and quadruple splitting δ = 0.75(1) mm s^{-1} points out the HS state of the Fe^{II} ion. Upon cooling down, another doublet appears, whose parameters (ΔE_Q = 0.69(1) mm s^{-1} and δ = 0.13(2) mm s^{-1}) correspond to the LS Fe^{II} ion. The ratio between doublets areas is close to 1:1, which indicates incomplete spin transition and corroborates well the magnetic data.

The Mössbauer spectrum of 2Ni-naph at 80 K consist of strong LS doublets with isomer shift values δ^{LS} = 0.49(2) mm s^{-1} and quadrupole splitting parameters ΔE_Q^{LS} = 0.24(1) mm s^{-1} (Figure 3b). Another minor doublet with a relative area of 8.9(2)% indicates an HS fraction with δ^{HS} = 1.36(1) mm s^{-1} and ΔE_Q^{HS} = 2.90(1) mm s^{-1}. Upon heating up to 150 K and

according to the transition of an Fe^{II} site to the HS state, the ratio between areas of the LS and HS doublets gets equal to 1:1 and the parameters of the doublets slightly change (δ^{LS} = 0.47(1) mm s^{-1} and ΔE_Q^{HS} = 0.18(0) mm s^{-1}; δ^{HS} = 1.16(1) mm s^{-1} and ΔE_Q^{HS} = 1.99(0) mm s^{-1}). Upon further heating up to 200 K, the spectrum contains two overlapping equally populated HS doublets with similar isomer shift values (δ^{HS1} = 1.13(1) mm s^{-1} and δ^{HS2} = 1.12(1) mm s^{-1}) and strongly different quadrupole splitting parameters (ΔE_Q^{HS1} = 1.72(2) mm s^{-1} and ΔE_Q^{HS2} = 1.09(1) mm s^{-1}). The ΔE_Q value is a very sensitive tool to probe local geometry around Fe^{II} ions.[16] At higher temperatures, the values reflect different geometric distortion of the corresponding coordination polyhedra, while at lower temperatures in the LS state the difference is relatively small, making the two different LS Fe^{II} ions undistinguishable. The deconvolution analysis data are collected in Table 1.

Table 1. Least-Squares-Fitted ^{57}Fe Mössbauer Spectra for 1Ag and 2Ni-naph

	T/K	doublet	ΔE_Q/mm s^{-1}	δ/mm s^{-1}	population
1Ag	80 K	LS	0.69(1)	0.13(2)	43.7(3)
		HS	1.01(0)	1.29(2)	56.3(4)
	200 K	HS	1.14(2)	0.75(1)	100
2Ni-naph	80 K	LS	0.49(1)	0.24(1)	91.1(2)
		HS	1.36(1)	2.90(1)	8.9(2)
	150 K	LS	0.47(1)	0.18(0)	51.3(2)
		HS	1.16(1)	1.99(0)	48.7(2)
	200 K	HS1	1.13(1)	1.72(2)	46.6(3)
		HS2	1.12(1)	1.09(1)	53.4(3)

Calorimetric Studies. Differential scanning calorimetric (DSC) measurements performed on the loaded samples reveal the anomalous heat capacity ΔC_p associated with the spin transitions. For 2Ni-naph, only the high-temperature transition could be recorded due to limitation of the temperature window of the calorimeter. Figure 4 shows ΔC_p vs T plots, and Table 2 gathers relevant thermodynamic parameters extracted from them, namely enthalpy (ΔH), entropy (ΔS), average variations, and average critical temperatures ($T_{ci}\downarrow + T_{ci}\uparrow/2$). The critical temperatures obtained from magnetic measurements agree reasonably well with those obtained from the maxima of ΔC_p vs T plots. The overall ΔH and ΔS values are, respectively, in the ranges 16−22 kJ mol^{-1} and 70−109 J K^{-1} mol^{-1} and are consistent with values typically observed in Hofmann-like clathrates of Fe^{II} featuring strong cooperative SCO behavior.[11]

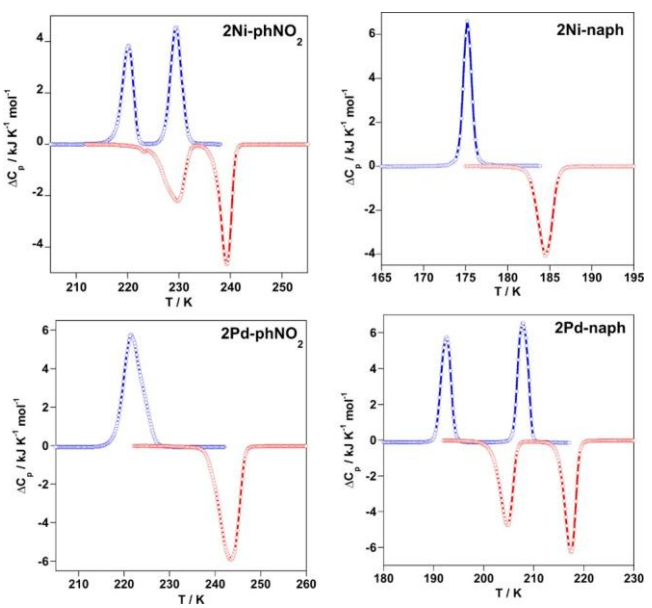

Figure 4. Anomalous heat capacity (DSC) for 2M-Guest (M = Ni, Pd; Guest = naphthalene, nitrobenzene). Blue and red curves correspond to the cooling and heating modes, respectively.

Single Crystal X-ray Studies. Single crystals of the title compounds were prepared using the slow diffusion method. The crystal structure determination was carried out at several temperatures to characterize the compounds in different spin states. Compound 1Ag crystallizes in the tetragonal $I4_122$ space group and 2Ni-phNO$_2$ in monoclinic space group $P2/m$, whereas 2Ni-naph, 2Pd-naph, and 2Pd-phNO$_2$ share the same triclinic space group $P\bar{1}$, similarly to 2Pt-naph and 2Pt-phNO$_2$.[13] Tables 3−5 contain the crystallographic data and selected distances and angles.

Structure of 1Ag. The crystal structure of 1Ag was determined at 120 and 250 K. The Fe^{II} sites define slightly elongated [FeN$_6$] octahedrons centered at the crossing point of two perpendicular binary axes bisecting the equatorial N−Fe−N angles (Table 4). The four equatorial positions are occupied by four equivalent $[Ag(CN)_2]^-$ units while the axial positions are occupied by the pyridine groups of the bpb ligand. At 250 K, the axial and equatorial bond lengths are 2.212(5) Å and 2.189(4) Å and decrease by 0.063 and 0.061 Å, respectively, at 120 K. The Fe−N bond lengths at 250 K are consistent with the Fe^{II} in the HS state; however, the shortening of these lengths suggests a very incomplete HS-to-LS conversion at 120 K. The CN moieties of the $[Ag(CN)_2]^-$ groups are slightly tilted (10.6°) with respect to the C−Ag−C axis and do not change significantly with temperature. The Fe^{II} sites are equatorially linked by the $[Ag(CN)_2]^-$ groups, thus generating slightly undulating $\{[FeAg(CN)_2]_4\}_n$ 2D grids. The windows of the $\{[FeAg(CN)_2]_4$ units are rhombus-like with distances between Fe^{II} ions of 10.716 (10.621) Å and angles 102.1°/77.8° (102.6°/77.4°) at 250 (120) K. The bpb ligands act as pillars connecting the Fe^{II} centers of consecutive layers defining a distorted α-Po type framework generated by tessellation of parallelepipeds $\{[FeAg(CN)_2]_8(bpb)_4\}$ (Figure 5a). The interlayer separation, measured between two Fe^{II} centers linked by bpb, is 16.681 (16.581) Å at 250 (120) K. Furthermore, three other identical frameworks are passing through the windows of the grid (Figure 5b). Consequently, the crystal structure of 1Ag is made up of four identical 3D networks interlocked in an unusual way. There are two different pairs of interpenetrated networks represented in Figure 5b with different colors, i.e., yellow and red (set 1) and green and blue (set 2). The nodes (Fe centers) of the parallelepipeds of one framework are placed on the barycenter of the parallelepipeds of the other framework belonging to the same set, in a similar way as described for other $\{Fe(L)[M^I(CN)_2]_2\}$ compounds. Within a set, the $\{[FeAg(CN)_2]_8(bpb)_4\}$ units are oriented in the same direction while the units of the different sets are orthogonally oriented.

The compactly packed crystal components exhibit short-distance interatomic contacts. The pyridine rings of neighbor concatenated networks exhibit strong π−π stacking interactions with the distance of the shortest contact C1···C1^i being 3.244(7) [3.304(8)] Å at 120 [250] K. The C≡N groups of neighbor networks form a C6···C6^i very short contact with a separation distance of 3.189(8) [3.226(8)] Å at 120 [250] K (i = x, 1 − y, 1

Table 2. Thermodynamic Parameters Calculated from Calorimetric (DSC) Measurements (ΔH/ kJ mol^{-1}; ΔS/J K^{-1} mol^{-1}; T_{ci}/K; ΔT_{ci}/K)

	ΔH_1^{av}	ΔS_1^{av}	T_{c1}^{av}	ΔT_{c1}	ΔH_2^{av}	ΔS_2^{av}	T_{c2}^{av}	ΔT_{c2}	ref.
Ni-naph	8.85	49.3	179.7	9.1					this work
Ni-phNO$_2$	8.53	36.4	234.2	9.5	7.60	32.2	225.0	10	this work
Pd-naph	12.00	56.5	212.5	9.6	10.42	52.4	198.8	11.3	this work
Pd-phNO$_2$	20.22	87.1	232.4	22.1					this work
Pt-naph	9.45	44.9	210.5	9.1	8.62	44.1	195.7	13.4	13
Pt-phNO$_2$	19.29	86.3	226.4	19.2					13

− z). Finally, Ag atoms exhibit weak argentophilic interactions with an Ag···Ag distance of 3.3778(2) [3.4299(3)] Å (Figure S4). As a consequence of the chiral crystal structure, the chains of Ag atoms form helices running along [001].

Structures of 2Ni-naph and 2Pd-naph. According to the magnetic properties, the structural analysis was carried out at three relevant temperatures where the crystals are HS (250 K), HS−LS [150 K 2Ni-naph; 204 K 2Pd-naph], and LS (120 K). Both compounds are isostructural, and the space group $P\bar{1}$ (triclinic) remains in the interval of temperatures investigated. There are two crystallographically distinct Fe^{II} centers (Fe1 and Fe2) lying on inversion centers defining elongated [FeN$_6$] octahedrons (Figure 6a). The equatorial positions are occupied by the CN groups of 4 equiv of [M^{II}(CN)$_4$]$^{2-}$ (M^{II} = Ni, Pd) counterions. Each [M(CN)$_4$]$^{2-}$ group connects four Fe^{II} centers defining slightly corrugated 2D {Fe[M(CN)$_4$]}$_n$ layers which stack along [001]. The axial positions of the Fe^{II} centers are occupied by the pyridyl groups of bpb, which pillar consecutive layers, thereby generating a 3D Hofmann SCO-MOF (Figure 6b) with large channels running along [100]. As already observed for the Pt compound, the bpb ligand is strongly bent, and the pyridine moieties are almost orthogonal to each other in Ni and Pd homologues, a fact that contrasts with the Ag complex.

At 120 K, the average Fe(1,2)−N bond lengths (⟨Fe−N⟩) are in the range 1.957−1.966 Å for both derivatives. These values are consistent with the LS state according to the magnetic data. At 150 K (Ni) and 204 K (Pd), the ⟨Fe1−N⟩ remains essentially unchanged, while ⟨Fe2−N⟩ experiences an increase of 0.198 Å (Ni) and 0.203 Å (Pd), which suggests the transformation of this site to the HS state. This is consistent with the plateau observed in the magnetic data at these temperatures. In this ordered mixed state, the Fe^{II} centers in the {Fe[M(CN)$_4$]}$_n$ layers define −LS−HS−LS− chains running along [010], while along [100] the chains display homogeneous spin states −HS−HS−HS− and −LS−LS−LS (Figure S5). In addition, the bpb ligands connect consecutive layers through Fe atoms with a distinct spin state (Figure S5). At 250 K, ⟨Fe1−N⟩ changes by 0.2 Å, attaining both compounds in the HS state. Interestingly, the N−Fe−N angles do not change significantly during the spin transition (Table 5).

The accessible guest free volume[17] of the SCO-MOF at 120 K is close to that observed for the Pt derivative, namely 809 and 846 Å^3 for Ni and Pd, respectively. This space is densely occupied by two crystallographically different naphthalene molecules. One, marked red in Figure 6b, is located halfway between the pyridine rings of the bpb ligand, coordinated to Fe1, while the other (lilac color) lies closer to the pyridine ring coordinated to Fe2. An important number of short contacts, smaller than the sum of the van der Waals radius of C (ca. 3.7 Å), are defined between the latter guest and the pyridine coordinated to Fe1 and Fe2 and the cyano groups of bpb (Figure 6c). Furthermore, there is an extended network of C···C short contacts between naphthalene molecules located in the channels running along [100] (Figure S6, Tables S2−S7). The number of host−guest and guest−guest intermolecular contacts decreases significantly as temperature increases due to thermal expansion and the change of volume associated with the population of the HS state.

Structures of 2Ni-phNO$_2$ and 2Pd-phNO$_2$. The structure of the host framework of both nitrobenzene clathrates is essentially the same as described for the naphthalene derivatives. The most relevant difference was found in 2Ni-phNO$_2$ since it crystallizes in the space group $P2/m$ (monoclinic) instead of $P\bar{1}$ (triclinic). Consequently, the sites Fe1 and Fe2 lie on inversion centers and on a plane of reflection which contains the pyridine group coordinated to the Fe1 and bisects the pyridine group coordinated to Fe2 (Figure 7a). Similarly to 2Pt-phNO$_2$, 2Pd-phNO$_2$ undergoes one step SCO while 2Ni-phNO$_2$ undergoes two-step SCO behavior with a small step, which could not be analyzed. At 120 K, ⟨Fe−N⟩ values for Fe1 and Fe2 sites, in the range 1.950−1.959 Å, are consistent with the LS state for both derivatives and increase around 0.205−0.215 Å at 295 K (2Ni-phNO$_2$) and 260 K (2Pd-phNO$_2$) as expected for a complete LS-to-HS transition (Table 5).

As in the precedent case, there are two crystallographically distinct guest molecules, which are organized in a similar way to that described for the naphthalene derivatives. One phNO$_2$ shows short contacts with the pyridine coordinated to Fe2 and one cyano moiety of bpb, while the other interacts with the pyridine coordinated to Fe1 (Figure 7b,c; see Tables S2−S7)

CONCLUDING REMARKS

Self-assembly of Fe^{II}, the bpb ligand, and [Ag(CN)$_2$]$^-$ or [M^{II}(CN)$_4$]$^{2-}$ (M^{II} = Ni and Pd) counterions has afforded a new series of interesting examples of Hofmann-like SCO coordination polymers. Similar to other {Fe(L)[M^I(CN)$_2$]$_2$} related systems where L is a bismonodentate ligand (Scheme 1), the ligand bpb acts as a pillar between consecutive {Fe[Ag(CN)$_2$]$_2$}$_n$ layers defining a simple 3D open network with the topology of α-Po in 1Ag. Typically, this open network features wide windows defined by {FeM^I(CN)$_2$]}$_4$ rhombuses, which favors the growth of two identical interlocked {Fe(L)[M^I(CN)$_2$]$_2$} structures.[11] Their relative orientation can be viewed as the result of a parallel shift of the networks, which brings the nodes of one network to occupy the center of the parallelepipedic voids of the other network (see yellow-red or blue-green pair in Figure 5). However, this situation is much more complex in 1Ag since there is enough space for a second subset of doubly interpenetrated networks, which, in addition, is orthogonally interlocked to the first subset (see Figure 5). This unprecedented situation stems from the increase of separation between the {Fe[M^I(CN)$_2$]$_2$}$_n$ layers, which is determined by the distance Fe(HS)−L−Fe(HS). This separation is 1.18, 1.055, 0.961, and 0.836 Å shorter for L = bipytz,[12a] bipydz,[12a] bpp,[12b] and dpb,[12c] respectively, than observed for L = bpb (16.681 Å; see Scheme 1). Other consequences of this singular interpenetration are the

Table 3. Crystallographic Parameters for 1Ag and 2M-Guest (M^{II} = Ni, Pd; Guest = Naphthalene, Nitrobenzene)

	1Ag		2Ni-naph			2Ni-phNO$_2$		2Pd-naph			2Pd-phNO$_2$	
temperature (K)	120(2)	250(2)	120(1)	150(1)	250(1)	120(1)	295(1)	120(1)	204(1)	250(1)	120(1)	260(1)
empirical formula	$C_{18}H_8Ag_2FeN_6$		$C_{38}H_{24}N_6NiFe$			$C_{30}H_{18}N_8O_4NiFe$		$C_{38}H_{24}N_6PdFe$			$C_{30}H_{18}N_8O_4PdFe$	
Mr	579.89		679.19			669.08		726.88			716.77	
crystal system	tetragonal		triclinic			monoclinic		triclinic			triclinic	
space group	$I4_122$		$P\bar{1}$			$P2/m$		$P\bar{1}$			$P\bar{1}$	
crystal size (mm)	0.20 × 0.17 × 0.06		0.04 × 0.06 × 0.06			0.05 × 0.08 × 0.15		0.04 × 0.08 × 0.08			0.03 × 0.05 × 0.08	
a (Å)	11.7245 (3)	11.7951 (5)	7.0404(3)	7.1878(5)	7.3262(5)	13.5575(8)	14.0178(6)	7.2261(5)	7.3789(4)	7.5133(7)	7.2355(4)	7.4860(2)
b (Å)			13.7679(7)	13.9259(13)	14.1439(6)	7.0586(3)	7.3240(4)	13.9453(8)	14.1403(7)	14.3298(10)	13.7948(7)	14.2688(4)
c (Å)	13.2791 (5)	13.4581 (11)	16.4902(8)	16.469(2)	16.3846(8)	15.6600(10)	15.7022(8)	16.3288(11)	16.3935(10)	16.193(2)	15.4309(10)	15.0260(6)
α (deg)			106.946(4)	74.782(8)	76.394(4)			106.288(5)	74.809(5)	102.716(7)	80.619(5)	86.069(3)
β (deg)			96.413(4)	82.112(6)	83.496(5)	100.703(2)	98.402(3)	96.496(5)	82.406(5)	95.108(8)	86.873(5)	84.010(3)
γ (deg)			90.009(4)	89.881(6)	89.942(4)			89.999(5)	89.939(5)	90.031(7)	89.870(5)	89.597(2)
V (Å^3)	1825.42 (12)	1872.3 (2)	1518.55(13)	1574.6(2)	1639.0(2)	1472.54(14)	1594.79(14)	1568.4(2)	1635.2(2)	1693.5(3)	1517.3(2)	1592.50(9)
Z	4		2			2		2			2	
D_c (mg cm^{-3})	2.110	2.057	1.485	1.432	1.376	1.509	1.393	1.539	1.476	1.425	1.569	1.495
F(000)	1112	1112	696			680		732			716	
μ (Mo K$_α$) (mm^{-1})	2.923	2.850	1.137	1.096	1.053	1.182	1.091	1.074	1.030	0.994	9.030	8.604
no. of total reflections	1533	1550	7635	7073	8300	3673	3950	7883	8180	8535	5992	6243
no. of reflections [$I > 2\sigma(I)$]	1397	1370	4969	3788	5252	2565	3181	6434	6632	5904	5174	5072
R [$I > 2\sigma(I)$][a]	0.0327	0.0376	0.0670	0.0772	0.0796	0.0678	0.0540	0.1174	0.0908	0.0782	0.0554	0.0385
R [all data][a]	0.0376	0.0441	0.1127	0.1566	0.1260	0.1073	0.0706	0.1327	0.1105	0.1154	0.0646	0.0858
S	1.019	1.055	0.939	0.917	1.117	1.071	1.068	1.010	1.016	1.017	1.031	1.116

[a] $R = \Sigma \| F_0| - |F_c| / \Sigma |F_0|$.

DOI: 10.1021/acs.inorgchem.7b00639
Inorg. Chem. 2017, 56, 7038−7047

Table 4. Selected Bond Lengths [Å] and Angles [deg] for 1Ag

temperature (K)	120(2)	250(2)
Fe−N(1)	2.149(5)	2.212(5)
Fe−N(2)	2.128(4)	2.189(4)
⟨Fe−N⟩	2.135	2.197
N(1)−Fe−N(2)	86.07(13)	85.57(11)

drastic decrease of accessible volume and the highly incomplete SCO behavior exhibited by 1Ag. All attempts to avoid 4-fold interpenetration in 1Ag, for example trying to include guest molecules (such as naphthalene or nitrobenzene) in the pores during the diffusion process, were unsuccessful. Concerning the second aspect, we believe that incompleteness of the SCO in 1Ag is a consequence of structural frustration essentially stemming from the balance of two opposite forces, contraction of the networks due to thermal induced SCO, on one hand, and strong π−π interactions between the pyridine rings present in the HS structure, which supposedly become more repulsive as the temperature decreases, on the other hand (Figure S4).

The denser nature of the $\{Fe[M^{II}(CN)_4]\}_n$ grids prevents interpenetration of identical networks in the series $\{Fe(L)[M^{II}(CN)_4]\}\cdot$Guest, thus affording reliable porosity, a fact which is also true for L = bpb. Indeed, the length of bpb has afforded the highest effective loading capacity so far described for the family of Hofmann-like SCO-MOFs. The structure of the six 2M-Guest (M = Ni, Pd, Pt; Guest = naphthalene, nitrobenzene) clathrates is essentially the same. They are characterized by the presence of two crystallographically distinct Fe^{II} nodes joined through a bpb ligand, which is markedly curved. The three 2M-naph derivatives and 2Ni-phNO$_2$ undergo cooperative two-step SCO without a change of symmetry of the crystal.[18] The 2M-naph derivatives show well-defined LS−HS intermediate plateaus, while the plateau is quite narrow for 2Ni-phNO$_2$. In contrast, 2M-phNO$_2$ (M = Pd, Pt) displays strong cooperative spin transition in one step. The structural differences between the two Fe^{II} sites, based on the average ⟨Fe−N⟩ bond lengths are insignificant, more precisely on the order of magnitude of the standard deviations. The most remarkable difference between the two Fe^{II} sites are found in the second coordination sphere where the coordinated pyridyl rings and CN groups of bpb interact in a different way with the guest molecules through short intermolecular π−π contacts particularly at 120 K. In the 2M-naph series, the half 4-cyano-pyridyl moiety of bpb coordinated to the Fe1 node exhibits a larger number of short contacts with the naphthalene molecules than the other half 4-cyano-pyridyl moiety of bpb coordinated to the Fe2 node (Figure 6 and Tables S2−S7). This difference seems to be at the heart of the larger stabilization of the LS state observed for the Fe1 nodes and, hence, of the formation of the ordered intermediate −Fe2(HS)−Fe1(LS)−Fe2(HS)− phase at the plateau. The thermal stability of this intermediate state decreases drastically when moving from the Ni^{II} derivative (ca. 40 K wide) to Pd^{II} and Pt^{II} (ca. 7−9 K wide) derivatives. This fact can be rationalized considering the larger number of intermolecular contacts observed for the Ni^{II} derivative, a fact which is consistent with the smaller ionic radius of Ni^{II} and, consequently, with the smaller unit cell volume relative to its Pd^{II} and Pt^{II} counterparts. The same arguments are valid for explaining the differences in thermal stability of the plateau between the 2M-phNO$_2$ and the 2M-naph series. The drastic decrease of host−guest contacts when replacing naphthalene with nitrobenzene is reflected on the destabilization of the intermediate plateau in 2M-phNO$_2$, which indeed is only observed for 2Ni-phNO$_2$ (ca. 4 K wide). Most likely, the stability of this plateau depends on a subtle and elusive combination of electronic (electron withdrawing-donating) and mechanical (elastic interactions) effects taking place between the bridging bpb molecule and the guest, which influence the HS−LS energy gap of the Fe^{II} centers.

Another relevant finding is the stabilization of the HS state of the guest-free 2M species in the whole range of temperatures. However, the lack of guest molecules seems not to perturb too much the porous framework 2M since its XRPD pattern is not significantly distinct to that of 2M-Guest. Indeed, the 2M series undergoes thermal induced SCO behavior at pressures of about 8 kbar, thus confirming that the coordination core of the Fe^{II} centers is similar to that of 2M-Guest. The lack of SCO in the 2M series strongly contrasts with the related Hofmann SCO-MOFs $\{Fe(pz)[M^{II}(CN)_4]\}$,[5] $\{Fe(azpy)[M^{II}(CN)_4]\}$,[7] and $\{Fe(bpac)[M^{II}(CN)_4]\}$,[19] which remain SCO at ambient pressure in the unloaded form. Interestingly, we also observe that up to ca. 10% of the ligand bpb is "auto-included" in the pores when no guest molecules other than solvents (methanol, water, etc.) are present in the synthesis. Autoinclusion of this small amount of bpb ligand in 2M explains the very residual gradual spin crossover feature observed in this series at relatively low temperatures.

Table 5. Selected Bond Lengths [Å] and Angles [deg] for 2M-Guest (M^{II} = Ni, Pd; Guest = Naphthalene, Nitrobenzene)

	2Ni-naph			2Ni-phNO$_2$		2Pd-naph			2Pd-phNO$_2$	
	120(1)	150(1)	250(1)	120(1)	295(1)	120(1)	204(1)	250(1)	120(1)	260(1)
Fe(1)−N(1)	2.002(4)	2.000(5)	2.205(4)	1.997(5)	2.206(4)	2.003(9)	2.008(6)	2.200(5)	1.993(4)	2.192(4)
Fe(1)−N(2)	1.942(4)	1.941(5)	2.139(4)	1.936(4)	2.145(3)	1.936(8)	1.943(6)	2.148(5)	1.933(4)	2.154(3)
Fe(1)−N(6)	1.946(4)	1.954(5)	2.153(4)			1.948(8)	1.947(6)	2.145(5)	1.929(4)	2.145(3)
⟨Fe(1)−N⟩	1.963	1.965	2.166	1.956	2.165	1.962	1.966	2.164	1.952	2.164
Fe(2)−N(3)	1.944(4)	2.139(5)	2.141(4)	1.938(4)	2.138(3)	1.934(8)	2.124(7)	2.130(5)	1.928(4)	2.140(3)
Fe(2)−N(4)	1.952(4)	2.127(5)	2.140(4)	2.001(6)	2.217(4)	1.937(8)	2.129(6)	2.133(5)	1.933(4)	2.143(3)
Fe(2)−N(5)	2.002(4)	2.225(5)	2.222(4)			1.999(9)	2.227(7)	2.224(6)	1.988(4)	2.211(4)
⟨Fe(2)N⟩	1.966	2.164	2.168	1.959	2.164	1.957	2.160	2.162	1.950	2.165
N(1)−Fe(1)−N(2)	88.1(2)	88.5(2)	87.8(2)	87.6(2)	88.13(10)	88.9(4)	88.9(2)	88.0(2)	88.3(2)	88.14(13)
N(1)−Fe(1)−N(6)	88.0(2)	87.9(2)	88.4(2)			88.2(4)	88.4(2)	88.5(2)	88.2(2)	88.35(13)
N(2)−Fe(1)−N(6)	89.3(2)	88.4(2)	89.7(2)			88.8(3)	87.5(2)	89.6(2)	88.8(2)	89.47(13)
N(3)−Fe(2)−N(4)	89.9(2)	89.6(2)	88.9(2)	89.2(2)	89.34(11)	89.2(3)	89.7(2)	89.1(2)	89.8(2)	89.75(13)
N(3)−Fe(2)−N(5)	89.1(2)	89.3(2)	89.3(2)			89.5(4)	89.0(3)	89.9(2)	89.8(2)	88.14(14)
N(4)−Fe(2)−N(5)	89.3(2)	89.2(2)	89.0(2)			88.4(4)	89.6(3)	88.8(2)	88.8(2)	89.52(14)

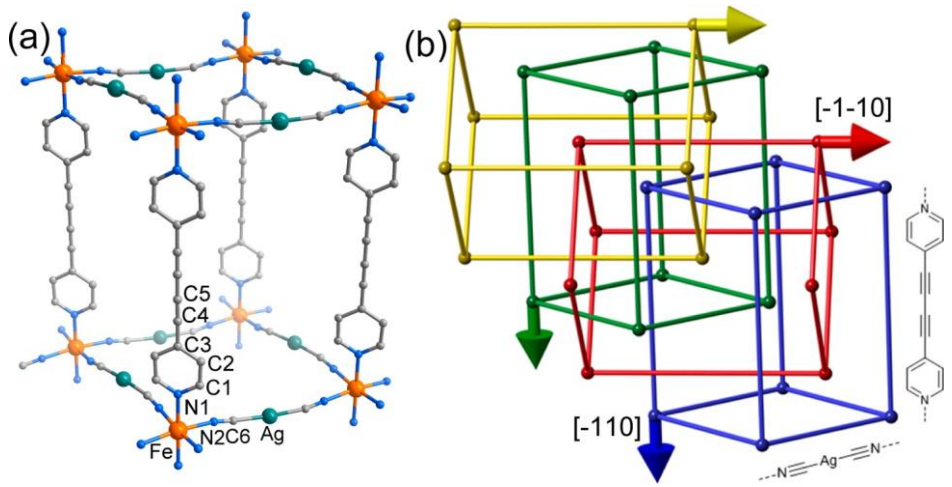

Figure 5. (a) Projection of a parallelepiped fragment of the 3D polymeric frameworks of 1Ag. (b) Schematically shown 4-fold concatenation of independent 3D polymeric networks. Arrows indicate the relative orientation of the $\{[FeAg(CN)_2]_8(bpb)_4\}$ units.

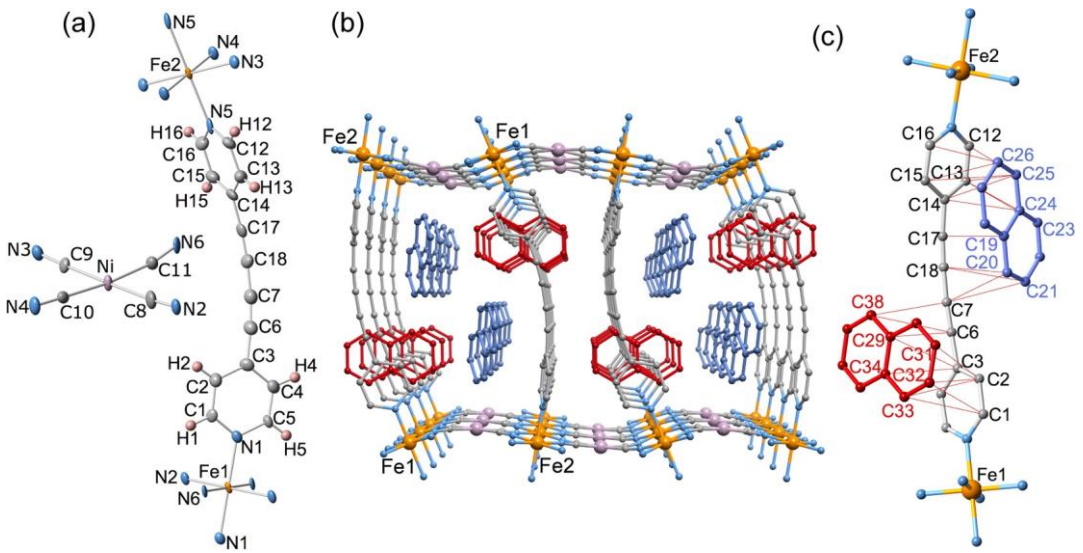

Figure 6. (a) ORTEP representation of relevant molecular fragments of 2Ni-naph at 120 K. Atom numbering is the same for 2Pd-naph (thermal ellipsoids are represented at 50% probability). (b) Projection of the framework down to [100]. Crystallographically distinct naphtalene guest molecules are denoted in red and lilac. (c) Short C···C contacts between naphthalene and bpb at 120 K (red lines correspond to C···C distances smaller than 3.7 Å).

EXPERIMENTAL

SECTION

Physical Measurements. Variable-temperature magnetic susceptibility data were recorded with a Quantum Design MPMS2 SQUID magnetometer equipped with a 7 T magnet, operating at 1 T and at temperatures 1.8−400 K. Experimental susceptibilities were corrected for diamagnetism of the constituent atoms by the use of Pascal's constants. Magnetic measurements under pressure were performed on 2M (M = Ni, Pd, Pt) operating at 1 T in the temperature interval 1.8−300 K using a hydrostatic pressure cell made of hardened beryllium bronze with silicon oil as the pressure transmitting medium and operating over the pressure range 1 bar to 10 kbar. The compounds were packed in a cylindrically shaped sample holder (1 mm in diameter and 5−7 mm in length) made up of very thin aluminum foil. The pressure was calibrated using the transition temperature of a superconducting lead of high-purity 99.999%. TGA measurements were performed on a Mettler Toledo TGA/SDTA 851e, in the 150−400 K temperature range under a nitrogen atmosphere with a rate of 10 K min^{-1}. Analyses for C, H, and N were performed after combustion at 850 °C using IR detection and gravimetry by means of a Perkin−Elmer 2400 series II device. Powder X-ray measurements were performed on a PANalytical

Empyrean X-ray powder diffractometer (monochromatic Cu K_α radiation).

Single Crystal X-ray Diffraction. Single-crystal X-ray data were collected on an Oxford Diffraction Supernova diffractometer using graphite monochromated Mo Kα radiation (λ = 0.71073 Å). A multiscan absorption correction was performed. The structures were solved by direct methods using SHELXS-2014 and refined by full-matrix least-squares on F^2 using SHELXL-2014.[20] Non-hydrogen atoms were refined anisotropically, and hydrogen atoms were placed in calculated positions refined using idealized geometries (riding model) and assigned fixed isotropic displacement parameters. For 2Ni-naph, some hydrogen atoms could not be located at 250 K due to thermal disorder in one of two independent naphthalene molecules (source alert type B). Similarly, nitrobenzene guest molecules show thermal disorder at 120 K (alert B) for 2Ni-phNO_2, which becomes stronger at 295 K (alerts A and B). Similarly some disorder in the nitrobenzene of 2Pd-phNO_2 induces one alert type B at 260 K, but the crystals deteriorate upon the spin transition, and residual density without chemical significance (3.32−2.57 e$Å^3$) is found at 120 K close to the Pd atom. Disorder of guest and residual electron density (2.10−1.90 e$Å^3$) located very close to the Pd atom is found for 2Pd-naph due to the low quality of the crystals (alerts A and B). However, the structures of the host frameworks as well as in

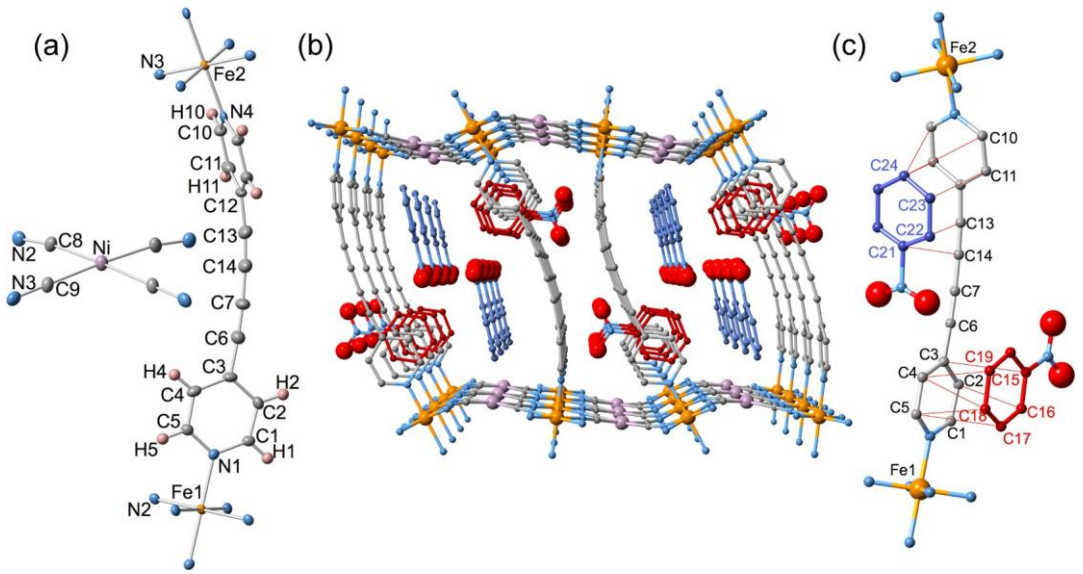

Figure 7. (a) ORTEP representation of relevant molecular fragments of 2Ni-phNO$_2$ at 120 K (thermal ellipsoids are represented at 50% probability). (b) Projection of the framework down to [100]. Crystallographically distinct nitrobenzene guest molecules are denoted in red and lilac. (c) Short C···C contacts between nitrobenzene and bpb at 120 K (red lines correspond to C···C distances smaller than 3.7 Å).

general those of the guest molecules are reasonably well determined. More importantly, they fully convey all the chemical and structural meaning required to explain correctly the spin crossover behavior in this series of compounds and compare well with the data reported previously for other members of the Hofmann-type spin crossover clathrate family. Supplementary crystallographic CIF data [1Ag at 120 K (CCDC-1550073) and 250 K (CCDC-1550074); 2Ni-naph at 120 K (CCDC-1550075), 150 K (CCDC-1550084), and 250 K (CCDC-1550076); 2Pd-naph at 120 K (CCDC-1550077), 204 K (CCDC-1550078), and 250 K (CCDC-1550083); 2Pd-phNO$_2$ at 120 K (CCDC-1550079) and 260 K (CCDC-1550080); 2Ni-phNO$_2$ at 295 K (CCDC-1550081) and 120 K (CCDC-1550082)] can be obtained free of charge from the Cambridge Crystallographic Data Centre.

Synthesis. All chemicals were purchased from commercial suppliers and used without further purification. Ligand bpb was synthesized according to the procedure reported elsewhere.[21]

Synthesis of 2Ni, 2Pd, and 2Pt. Microcrystalline samples were prepared in an Ar atmosphere by adding dropwise water−methanolic solution of $K_2[M^{II}(CN)_4]$ (M^{II} = Ni, Pd, or Pt; 0.2 mmol, 5 mL) to a methanolic solution containing $Fe(BF_4)_2{\cdot}6H_2O$ (0.4 mmol, 3 mL) and bpb (0.4 mmol) under vigorous stirring. The resulting red (2M) solid was stirred for 15 min, filtered, washed with water, and dried in the air (yield ca. 85%). EDX analysis (energy dispersive X-ray analysis) confirmed the stoichiometry of bimetallic compounds: Fe/Ni or Fe/Pd or Fe/Pt = 1:1. Elemental analysis (%) for 2Ni ($C_{20.14}H_{12.8}N_{6.2}OFeNi$): C, 51.17; H, 2.44; N, 18.30. Found: C, 51.55; H, 2.71; N, 18.27. Elemental analysis (%) for 2Pd ($C_{20.14}H_{12.8}N_{6.2}OFePd$): C, 46.85; H, 2.47; N, 16.60. Found: C, 46.86; H, 2.14; N, 16.73. Elemental analysis (%) for 2Pt ($C_{20.14}H_{12.8}N_{6.2}OFePt$): C, 40.06; H, 2.11; N, 14.20. Found: C, 39.97; H, 1.99; N, 14.01.

Synthesis of 2Ni-naph, 2Ni-phNO$_2$, 2Pd-naph, 2Pd-phNO$_2$, and 1Ag. Single crystals of the compounds were grown using a slow diffusion technique. A three-arm tube, containing in one arm $(NH_4)_2Fe(SO_4)_2{\cdot}6H_2O$ (20 mg, 51 mmol) dissolved in water (0.5 mL), in the second arm solid bpb (11 mg, 49 mmol) and guest (50 mg), and in the third arm $K_2Ni(CN)_4{\cdot}3H_2O$ or $K_2Ni(CN)_4{\cdot}H_2O$ (51 mmol) in water (0.5 mL), was carefully filled with a water/methanol (1:1) solution and sealed with parafilm. Square shaped yellow (2Ni-naph, 2Ni-phNO$_2$, and 2Pd-naph) or brown (2Pd-phNO$_2$) crystals suitable for single crystal X-ray analysis were obtained in 6 weeks with a yield of ca. 20%. EDX analysis (energy dispersive X-ray analysis) confirmed the stoichiometry of bimetallic compounds: Fe/Ni or Fe/Pd = 1:1, Fe/Ag = 1:2.

Elemental analysis (%) for 1Ag ($C_{18}H_8Ag_2FeN_6$) calcd: C, 37.28; H, 1.39; N, 14.49. Found: C, 36.74; H, 1.35; N, 14.33. Elemental analysis (%) for 2Ni-naph ($C_{38}H_{24}FeN_6Ni$): calcd: C, 67.20; H, 3.56; N, 12.37. Found: C, 65.75; H, 3.48; N, 12.06. Elemental analysis (%) for 2Ni-phNO$_2$ ($C_{30}H_{18}FeN_8O_4Ni$) calcd: C, 53.86; H, 2.71; N, 16.75. Found: C, 52.65; H, 2.64; N, 16.28. Elemental analysis (%) for 2Pd-naph ($C_{38}H_{24}FeN_6Pd$) calcd: C, 62.79; H, 3.33; N, 11.56. Found: C, 61.66; H, 3.25; N, 11.33. Elemental analysis (%) for 2Pd-phNO$_2$ ($C_{30}H_{18}FeN_8O_4Pd$) calcd: C, 50.27; H, 2.53; N, 15.63. Found: C, 49.61; H, 2.47; N, 15.29.

ASSOCIATED CONTENT

Supporting Information

The Supporting Information is available free of charge on the ACS Publications website at DOI: 10.1021/acs.inorgchem.7b00639.

Thermal analyses (Figure S1 and S2); powder X-ray diffraction (Figure S3); different views of the 1Ag structure (Figure S4); views of the structures 2Ni-naph and 2Pd-naph (Figures S5 and S6); critical temperatures obtained from magnetic data (S1); intermolecular contacts for 2Ni-naph, 2Ni-phNO$_2$, 2Pd-naph, and 2Pd-phNO$_2$ (Tables S2−S7) (PDF)

Accession Codes

CCDC 1550073−1550084 contain the supplementary crystallographic data for this paper. These data can be obtained free of charge via www.ccdc.cam.ac.uk/data_request/cif, or by emailing data_request@ccdc.cam.ac.uk, or by contacting The Cambridge Crystallographic Data Centre, 12 Union Road, Cambridge CB2 1EZ, UK; fax: +44 1223 336033.

AUTHOR INFORMATION

Corresponding Authors

*E-mail: maksym.Seredyuk@uv.es.

*E-mail: jose.a.real@uv.es.

ORCID

Matti Haukka: 0000-0002-6744-7208

José Antonio Real: 0000-0002-2302-561X

Notes

The authors declare no competing financial interest.

ACKNOWLEDGMENTS

We thank the Spanish Ministerio de Economía y Competitividad (MINECO) and FEDER funds (CTQ2013-46275-P and CTQ2016-78341-P and Unidad de Excelencia Mariade Maeztu MDM-2015-0538) and Generalitat Valenciana (PROMETEO/2016/147). L.P.-L. and F.J.V.-M. thank, respectively, the Universidad de Valencia and MINECO for a predoctoral FPI grant.

REFERENCES

(1) Sato, O. Nat. Chem. 2016, 8, 644−656.

(2) (a) König, E. Nature and Dynamics of the Spin-State Interconversion in Metal-Complexes. Struct. Bonding (Berlin, Ger.) 1991, 76, 51−152. (b) Gütlich, P.; Hauser, A.; Spiering, H. Thermal and Optical Switching of Iron(II) Complexes. Angew. Chem., Int. Ed. Engl. 1994, 33, 2024−2054. (c) Real, J. A.; Gaspar, A. B.; Niel, V.; Muñoz, M. C. Communication between Iron(II) Building Blocks in Cooperative Spin Transition Phenomena. Coord. Chem. Rev. 2003, 236, 121−141. (d) Gütlich, P.; Goodwin, H. A. Spin Crossover in Transition Metal Compounds I-III. Top. Curr. Chem.; Springer: Berlin, 2004; Vols. 233−235. (e) Real, J. A.; Gaspar, A. B.; Muñoz, M. C. Thermal, Pressure and Light Switchable Spin-Crossover Materials. Dalton Trans. 2005, 2062−2079. (f) Bousseksou, A.; Molnar, G.; Salmon, L.; Nicolazzi, W. Molecular Spin Crossover Phenomenon: Recent Achievements and Prospects. Chem. Soc. Rev. 2011, 40, 3313−3335. (g) Halcrow, M. A. Spin-crossover materials: properties and applications; John Wiley & Sons: Hoboken, NJ, 2013.

(3) (a) García, Y.; Niel, V.; Muñoz, M. C.; Real, J. A. Top. Curr. Chem. 2004, 233, 229−257. (b) Muñoz, M. C.; Real, J. A. Polymeric Spin-Crossover Materials. Spin-Crossover Materials: Properties and Applications; Halcrow, M. A., Ed.; John Wiley & Sons: Hoboken, NJ, 2013; pp 121−139.

(4) (a) Niel, V.; Martinez-Agudo, J. M.; Muñoz, M. C.; Gaspar, A. B.; Real, J. A. Cooperative Spin Crossover Behavior in Cyanide-Bridged Fe(II)-M(II) Bimetallic 3D Hofmann-like Networks (M = Ni, Pd, and Pt). Inorg. Chem. 2001, 40, 3838−3839. (b) Niel, V.; Muñoz, M. C.; Gaspar, A. B.; Galet, A.; Levchenko, G.; Real, J. A. Thermal-, Pressure-, and Light-Induced Spin Transition in Novel Cyanide-Bridged Fe^{II}-Ag^{I} Bimetallic Compounds with Three-Dimensional Interpenetrating Double Structures $\{Fe^{II}L_x[Ag(CN)_2]_2\}\cdot G$. Chem. - Eur. J. 2002, 8, 2446−2453.

(5) Ohba, M.; Yoneda, K.; Agustí, G.; Muñoz, M. C.; Gaspar, A. B.; Real, J. A.; Yamasaki, M.; Ando, H.; Nakao, Y.; Sakaki, S.; Kitagawa, S. Bidirectional Chemo-Switching of Spin State in a Microporous Framework. Angew. Chem., Int. Ed. 2009, 48, 4767−4771.

(6) Muñoz-Lara, F. J.; Gaspar, A. B.; Muñoz, M. C.; Arai, M.; Kitagawa, S.; Ohba, M.; Real, J. A. Sequestering Aromatic Molecules with a Spin-Crossover Fe^{II} Microporous Coordination Polymer. Chem. - Eur. J. 2012, 18, 8013−8018.

(7) Agustí, G.; Cobo, S.; Gaspar, A. B.; Molnar, G.; Moussa, N. O.; Szilagyi, P. A.; Palfi, V.; Vieu, C.; Muñoz, M. C.; Real, J. A.; Bousseksou, A. Thermal and Light-Induced Spin Crossover Phenomena in New 3D Hofmann-Like Microporous Metalorganic Frameworks Produced As Bulk Materials and Nanopatterned Thin Films. Chem. Mater. 2008, 20, 6721−6732.

(8) Bartual-Murgui, C.; Ortega-Villar, N. A.; Shepherd, H. J.; Muñoz, M. C.; Salmon, L.; Molnar, G.; Bousseksou, A.; Real, J. A. Enhanced porosity in a new 3D Hofmann-like network exhibiting humidity sensitive cooperative spin transitions at room temperature. J. Mater. Chem. 2011, 21, 7217−7222.

(9) Muñoz-Lara, F. J.; Gaspar, A. B.; Muñoz, M. C.; Ksenofontov, V.; Real, J. A. Novel Iron(II) Microporous Spin-Crossover Coordination Polymers with Enhanced Pore Size. Inorg. Chem. 2013, 52, 3−5.

(10) Sciortino, N. F.; Scherl-Gruenwald, K. R.; Chastanet, G.; Halder, G. J.; Chapman, K. W.; Letard, J.-F.; Kepert, C. J. Hysteretic Three-Step Spin Crossover in a Thermo- and Photochromic 3D Pillared Hofmann-type Metal−Organic Framework. Angew. Chem., Int. Ed. 2012, 51, 10154−10158.

(11) (a) Muñoz, M. C.; Real, J. A. Thermo-, Piezo-, Photo- and Chemo-Switchable Spin Crossover Iron(II)-Metallocyanate Based Coordination Polymers. Coord. Chem. Rev. 2011, 255, 2068−2093. (b) Ni, Z.-P.; Liu, J.-L.; Hoque, Md. N.; Liu, W.; Li, J.-Y.; Chen, Y.-C.; Tong, M.-L. Recent advances in guest effects on spin-crossover behavior in Hofmann-type metal-organic frameworks. Coord. Chem. Rev. 2017, 335, 28−43.

(12) (a) Clements, J. E.; Price, J. R.; Neville, S. M.; Kepert, C. J. Perturbation of Spin Crossover Behavior by Covalent Post-Synthetic Modification of a Porous Metal−Organic Framework. Angew. Chem., Int. Ed. 2014, 53, 10164−10168. (b) Li, J.-Y.; Chen, Y.-C.; Zhang, Z.-M.; Liu, W.; Ni, Z.-P.; Tong, M.-L. Tuning the Spin-Crossover Behaviour of a Hydrogen-Accepting Porous Coordination Polymer by Hydrogen-Donating Guests. Chem. - Eur. J. 2015, 21, 1645−1651. (c) Li, J.-Y.; He, C.-T.; Chen, Y.-C.; Zhang, Z.-M.; Liu, W.; Ni, Z.-P.; Tong, M.-L. Tunable cooperativity in a spin-crossover Hoffman-like metal-organic framework material by aromatic guests. J. Mater. Chem. C 2015, 3, 7830−7835. (d) Gural'skiy, I. A.; Golub, B. O.; Shylin, S. I.; Ksenofontov, V.; Shepherd, H. J.; Raithby, P. R.; Tremel, W.; Fritsky, I. O. Cooperative High-Temperature Spin Crossover Accompanied by a Highly Anisotropic Structural Distortion. Eur. J. Inorg. Chem. 2016, 2016, 3191−3195. (e) Valverde-Muñoz, F. J.; Seredyuk, M.; Muñoz, M. C.; Znovjyak, K.; Fritsky, I. O.; Real, J. A. Strong Cooperative Spin Crossover in 2-D and 3-D Fe^{II}-$M^{I,II}$ Hofmann-like Coordination Polymers Based on 2-Fluoropyrazine. Inorg. Chem. 2016, 55, 10654−10665.

(13) Piñeiro-Lopez, L.; Seredyuk, M.; Muñoz, M. C.; Real, J. A. Two- and one-step cooperative spin transitions in Hofmann-like clathrates with enhanced loading capacity. Chem. Commun. 2014, 50, 1833−1835.

(14) Hauser, A. Light-Induced Spin Crossover and the High-Spin→Low-Spin Relaxation. Top. Curr. Chem. 2004, 234, 155−198.

(15) Letard, J. F. Photomagnetism of iron(II) spin crossover complexes-the T(LIESST) approach. J. Mater. Chem. 2006, 16, 2550−2559.

(16) Gütlich, P.; Bill, E.; Trautwein, A. X. Mossbauer spectroscopy and transition metal chemistry; Springer: Heidelberg, 2010.

(17) Spek, A. Structure validation in chemical crystallography. Acta Crystallogr., Sect. D: Biol. Crystallogr. 2009, 65, 148−155.

(18) Ortega-Villar, N.; Muñoz, M. C.; Real, J. A. Symmetry breaking in iron(II) spin-crossover molecular crystals. Magnetochemistry 2016, 2, 16−37.

(19) Bartual-Murgui, C.; Akou, A.; Shepherd, H. J.; Molnar, G.; Real, J. A.; Salmon, L.; Bousseksou, A. Tunable Spin-Crossover Behavior of the Hofmann-like Network $\{Fe(bpac)[Pt(CN)_4]\}$ through Host-Guest Chemistry. Chem. - Eur. J. 2013, 19, 15036−15043.

(20) Sheldrich, G. M. SHELXL 2014; University of Göttingen: Göttingen, Germany, 2014.

(21) Ciana, L. D.; Haim, A. J. Synthesis of 1,4-bis(4-pyridyl)butadiyne. J. Heterocycl. Chem. 1984, 21, 607−608.